eprints@whiterose.ac.uk
https://eprints.whiterose.ac.uk/

A High-Order Imaging Algorithm for High-Resolution Space-Borne SAR Based on a Modified Equivalent Squint Range Model

Pengbo Wang[1][2], Wei Liu[2], Jie Chen [1][*], Mu Niu[3], and Wei Yang[1]

[1]School of Electronic and Information Engineering, Beihang University, Beijing 100191, China
[2]Department of Electronic and Electrical Engineering, University of Sheffield, Sheffield S1 3JD, UK
[3]School of Mathematics and Statistics, University of Sheffield, Sheffield S1 3JD, UK

Abstract—Two challenges have been faced in signal processing of ultra-high resolution space-borne synthetic aperture radar (SAR). The first challenge is constructing a precise range model and the second one is to develop an efficient imaging algorithm since traditional algorithms fail to process ultra-high resolution space-borne SAR data effectively. In this paper, a novel high-order imaging algorithm for high resolution space-borne SAR is presented. Firstly, a modified equivalent squint range model (MESRM) is developed by introducing equivalent radar acceleration into the equivalent squint range model, and it is more suitable for high resolution space-borne SAR. The signal model based on the MESRM is also presented. Secondly, a novel high-order imaging algorithm is derived. The insufficient pulse repetition frequency (PRF) problem is solved by an improved sub-aperture method and accurate focusing is achieved through an extended hybrid correlation algorithm. Simulations are performed to validate the presented algorithm.

Index Terms—Synthetic aperture radar, Radar imaging, Imaging algorithm, Hybrid Correlation Algorithm.

I. INTRODUCTION

SINCE the first space-borne synthetic aperture radar (SAR) was launched in 1978 [1], [2], significant progress has been made in this area. The resolution of space-borne SAR has been upgraded from tens of meters to the meter level. Several advanced space-borne SAR systems, such as TerraSAR and Cosmo-SkyMed, have been in the orbit, with a resolution of 1m [3]–[11]. The TerraSAR next generation (TerraSAR NG) to be lunched in 2016, will reach a resolution of 0.25m [12], [13]. However, along with the improvement of resolution, a longer integration time of the signal is required, which poses many challenges for space-borne SAR signal processing, in particular the imaging part.

For traditional space-borne SAR systems, the integration time is less than 2 seconds, and the SAR motion can be well represented by the hyperbolic range equation model (HREM) or the equivalent squint range model (ESRM) [14]–[16]. Most of the classic SAR imaging algorithms, such as the range Doppler algorithm (RDA), the chirp scaling algorithm (CSA), the wavenumber domain algorithm (ωkA), and their variations, are all based on either HREM or ESRM. However,

for ultra-high resolution space-borne SAR systems, the much longer integration time will introduce significant phase errors in signal processing based on old range models. In order to solve this problem, Huang and Qiu proposed an advanced ESRM (A-ESRM) to describe the range history of MEO SAR [17], where an additional linear term is introduced into the conventional ESRM so that it can handle the focusing issue of an azimuth resolution around 3 m at an altitudes ranging from 1000 to 10000 km. However, the fourth and higher order phase errors could not be compensated in A-ESRM. A fourth-order Doppler range model (DRM4) for space-borne SAR imaging was proposed by Eldhuset [18]–[21], and a 2-D exact transfer function (ETF) was derived. Compared with the conventional hyperbolic range model, the third and fourth order phase errors can be fully compensated, and a better imaging result can be obtained. However, the model does not consider the effect of higher order phase errors, which limits its application in imaging processing. The method of series reversion (MSR) is another range model for space-borne SAR imaging [22], [23], where the range equation is expressed by a series expansion, and its accuracy is dependent on the number of terms used. To meet the requirement of ultra-high resolution space-borne SAR imaging, more than four terms in the expansion are needed, which results in a high complexity system.

In order to describe the range history more accurately in the high resolution case, a modified ESRM is proposed in this paper. The proposed model introduces equivalent radar acceleration into the ESRM. The range history can be accurately represented with an azimuth resolution up to 0.1m. Based on the modified ESRM, a novel high-order imaging algorithm is presented for ultra-high resolution space-borne SAR imaging, where improved sub-aperture processing is applied to remove azimuth aliasing, and accurate focusing is realized through an extended hybrid correlation algorithm. Extensive simulations are performed to show the significantly improved imaging result. This paper is organized as follows. With a brief description of ESRM, a modified ESRM is presented in Section II. The corresponding high-order imaging algorithm for high resolution space-borne SAR is developed in Section III. Simulation results are provided in Section IV and conclusions are drawn in Section V.
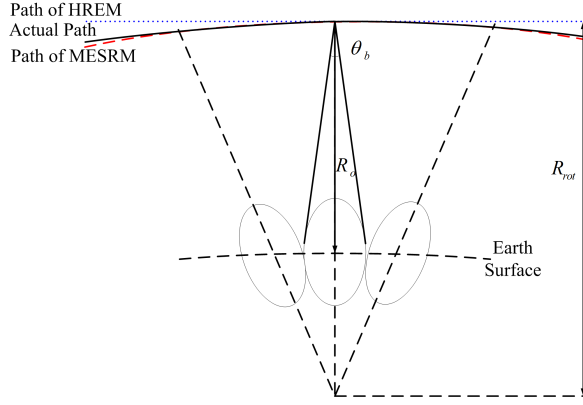
* Corresponding author: Jie Chen

Fig. 1. Geometry of a typical space-borne SAR.

Fig. 2. Phase error caused by range deviation as a function of azimuth resolution in conventional ESRM.

II. MODIFIED RANGE AND SIGNAL MODELS

A. Conventional ESRM

The space-borne SAR geometry in Earth-centered rotating coordinates is illustrated in Fig. 1, where the actual path is represented by the black solid line, and the paths based on HREM and MESRM are denoted by the blue dotted line and red dashed lines, respectively. The ESRM approximates the actual path of the satellite as a straight line, and its range equation can be expressed as

$$R(t, r_0) = \sqrt{r_0^2 + v_0^2 t^2 - 2r_0 v_0 t \cos\varphi_0} \ , \tag{1}$$

$$\begin{cases} v_0 = \sqrt{\left(\dfrac{\lambda f_d}{2}\right)^2 - \dfrac{\lambda r_0 f_r}{2}} \\ \varphi_0 = arccos\left(\dfrac{\lambda f_d}{2V_0}\right) \ , \end{cases} \tag{2}$$

$$f_d = -\frac{2\left(\mathbf{V}_{sat} - \mathbf{V}_{tar}\right) \cdot \left(\mathbf{R}_{sat} - \mathbf{R}_{tar}\right)}{\lambda r_0} \ , \tag{3}$$

$$f_r = -\frac{2\left(\mathbf{A}_{sat} - \mathbf{A}_{tar}\right) \cdot \left(\mathbf{R}_{sat} - \mathbf{R}_{tar}\right)}{\lambda r_0}$$
$$- \frac{2\left(\mathbf{V}_{sat} - \mathbf{V}_{tar}\right) \cdot \left(\mathbf{V}_{sat} - \mathbf{V}_{tar}\right)}{\lambda r_0} + \frac{\lambda f_d^2}{2r_0} \ , \tag{4}$$

where t is the azimuth time, r_0 is the slant range at Doppler center time, v_0 is the equivalent radar velocity between the scatterer and the SAR, φ_0 is the equivalent squint angle, f_d represents the Doppler centroid frequency, and f_r represents the azimuth FM rate, $\mathbf{R}$, $\mathbf{V}$, and $\mathbf{A}$ denote the position vector, velocity vector and acceleration vector, respectively. The subscript sat represents the satellite, and tar represents ground target.

It is clear from equations (1) and (2) that only the Doppler centroid and the azimuth FM rate are involved in the conventional ESRM, which is not sufficient for range history description of high resolution space-borne SAR. As the integration time increases, the range deviation between actual range history and the ESRM becomes significant. To show this, we perform a simple simulation with orbit parameters and radar parameters listed in Section IV. The maximal phase error caused by range deviation as a function of azimuth resolution is given in Fig. 2. The maximal phase error (blue solid line) caused by the conventional ESRM is greater than $\pi/4$ (red
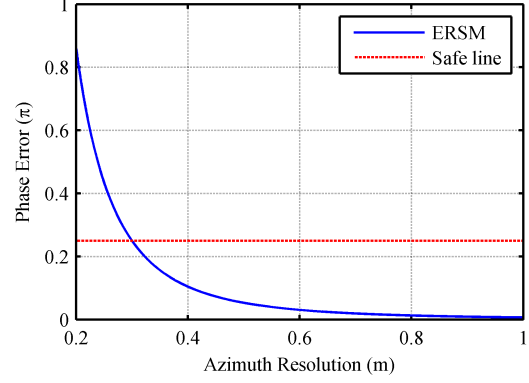
dashed lines), when the azimuth resolution is smaller than 0.3m. The resolution cannot meet the requirement of future applications, such as TerraSAR NG [12]. Therefore, a more accurate range model is needed.

B. Modified ESRM

In order to improve the precision of ESRM, the equivalent radar acceleration is introduced in the range equation, leading to a modified equivalent squint range model (MESRM) as follows (Note: the words "equivalent squint" is used to describe the effects of Earth's rotation)

$$R(t, r_0) = \sqrt{r_0^2 + \left(v_0 t + \frac{A_0 t^2}{2}\right)^2 - r_0 \left(2v_0 t + A_0 t^2\right) \cos\varphi_0} \ , \tag{5}$$

where A_0 is the equivalent radar acceleration.

To facilitate comparison, we expand equation (5) and obtain the following modified range equation

$$R(t, r_0) = \sqrt{r_0^2 + v_0'^2 t^2 - 2r_0 v_0' t \cos\varphi_0' + \Delta a_3 t^3 + \Delta a_4 t^4} \ , \tag{6}$$

where

$$\begin{cases} v_0' = \sqrt{v_0^2 - r_0 A_0 \cos\varphi_0} \\ \varphi_0' = arccos\left(\dfrac{v_0 \cos\varphi_0}{v_0'}\right) \\ \Delta a_3 = v_0 A_0 \\ \Delta a_4 = \dfrac{A_0^2}{4} \ . \end{cases} \tag{7}$$

Differentiating (6) with respect to t, We have

$$\frac{\partial R(t, r_0)}{\partial t} = -v_0' \cos\varphi_0' + \frac{v_0'^2 \sin\varphi_0'^2}{r_0} t + \Delta_2 t^2 + \Delta_3 t^3 + \cdots$$
$$= -\frac{\lambda f_d}{2} - \frac{\lambda f_r}{2} t - \frac{\lambda f_{r3}}{4} t^2 - \frac{\lambda f_{r4}}{12} t^3 + \cdots \ , \tag{8}$$

where

$$\Delta_2 = \frac{3\Delta a_3}{2r_0} + \frac{3v_0'^3 \sin\varphi_0'^2 \cos\varphi_0'}{2r_0^2} \ , \tag{9}$$

$$\Delta_3 = \frac{2\Delta a_4}{r_0} + \frac{2\Delta a_3 v_0' \cos\varphi_0'}{r_0^2} - \frac{v_0'^4 \sin\varphi_0'^2}{2r_0^3} \left(1 - 5\cos\varphi_0'^2\right) \ , \tag{10}$$
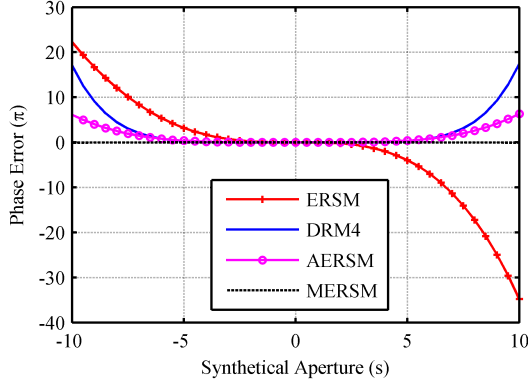
Fig. 3. Phase error caused by range deviation as a function of the synthetic aperture time in MESRM/ESRM/DRM4/AESRM.

$$f_{r3} = -\frac{2\left(\mathbf{A}'_{sat} - \mathbf{A}'_{tar}\right)\left(\mathbf{R}_{sat} - \mathbf{R}_{tar}\right)}{\lambda r_0}$$
$$-\frac{6\left(\mathbf{A}_{sat} - \mathbf{A}_{tar}\right)\left(\mathbf{V}_{sat} - \mathbf{V}_{tar}\right)}{\lambda r_0} + \frac{3\lambda f_d f_r}{2r_0}, \quad (11)$$

$$f_{r4} = -\frac{8\left(\mathbf{A}'_{sat} - \mathbf{A}'_{tar}\right)\left(\mathbf{V}_{sat} - \mathbf{V}_{tar}\right)}{\lambda r_0}$$
$$-\frac{6\left(\mathbf{A}_{sat} - \mathbf{A}_{tar}\right)\left(\mathbf{A}_{sat} - \mathbf{A}_{tar}\right)}{\lambda r_0} + \frac{3\lambda f_r^2}{2r_0} \quad (12)$$
$$-\frac{2\left(\mathbf{A}''_{sat} - \mathbf{A}''_{tar}\right)\left(\mathbf{R}_{sat} - \mathbf{R}_{tar}\right)}{\lambda r_0} + \frac{2\lambda f_d f_{r3}}{r_0},$$

where f_{r3} denotes the rate of the azimuth FM rate, f_{r4} denotes its second-order derivative, $\mathbf{A}'$ and $\mathbf{A}''$ represent the rate of the acceleration vector and its second-order derivative, respectively. Based on equation (8), the variables in (6) can be calculated by

$$\begin{cases} v'_0 = \sqrt{\left(\frac{\lambda f_d}{2}\right)^2 - \frac{\lambda r_0 f_r}{2}} \\ \varphi'_0 = arccos\left(\frac{\lambda f_d}{2v'_0}\right) \\ \Delta a_3 = \frac{-\lambda r_0 f_{r3}}{6} - \frac{v'^3_0 sin\varphi'^2_0 cos\varphi'_0}{r_0} \\ \Delta a_4 = \frac{-\lambda r_0 f_{r4}}{24} + \frac{v'^4_0 sin\varphi'^2_0}{4r_0^2}\left(1 - 5cos\varphi'^2_0\right) - \frac{\Delta a_3 v'_0 cos\varphi'_0}{r_0} . \end{cases} \quad (13)$$

From equations (6) and (13), it can be seen that the new model not only perfectly compensates the actual range history up to the quartic term, but also partially compensates the higher-order terms, which makes MESRM more suitable for the ultra-high resolution case. To show the improved accuracy of the new range model, the phase errors caused by range deviation as a function of the synthetic aperture time is provided in Fig. 3 with orbit parameters and radar parameters listed in Section IV. It can be seen clearly that MESRM is more accurate than ESRM and DRM4. Under the azimuth phase error criterion of 0.25π, the maximal synthetic aperture time for the ESRM and DRM4 is less than 9.6 s. However, with the proposed MESRM, the phase error is less than 0.06π even if the synthetic aperture time is up to 20 s. As a result, an azimuth resolution higher than 0.1 m can be achieved, which can meet the requirements of most future space-borne SAR applications.

C. Signal Model

Based on the MESRM, after demodulation to baseband, the received signal for a point target can be described as

$$S(\tau, t) = \sigma_0 \omega_a \left(t - t_0\right) \cdot exp\left\{-\frac{j4\pi R(t)}{\lambda}\right\}$$
$$\cdot \omega_r\left(\tau - \frac{2R(t)}{c}\right) \cdot exp\left\{j\pi K_r\left[\tau - \frac{2R(t)}{c}\right]^2\right\}, \quad (14)$$

where σ_0 represents the scattering coefficient, $\omega_r(\cdot)$ and $\omega_a(\cdot)$ denote antenna pattern functions in the range and azimuth directions, respectively, λ is the signal wavelength, c is the speed of light, K_r is the range chirp rate, τ is the fast time, and t_0 is the Doppler center time.

In order to obtain the 2D point target spectrum (PTS) of the above echo expression, the principle of stationary phase and Fourier transformation is used. The 2D PTS of the echo signal can be obtained as

$$S(f_\tau, f_a) = \sigma_0 \omega_a\left(t_a\left(f_a, f_\tau\right)\right) \cdot \omega_r\left(f_\tau\right)$$
$$\cdot exp\left\{-j4\pi\left(\frac{1}{\lambda} + \frac{f_\tau}{c}\right) R\left(t_a\left(f_a, f_\tau\right)\right)\right\} \quad (15)$$
$$\cdot exp\left\{-j2\pi f_a t_a\left(f_a, f_\tau\right)\right\} \cdot exp\left\{-\frac{j\pi f_\tau^2}{K_r}\right\},$$

where f_τ is the range frequency, f_a is the azimuth frequency, and $t_a(\cdot)$ is the stationary point, obtained by solving the following equation

$$2\left(\frac{1}{\lambda} + \frac{f_\tau}{c}\right)\frac{\partial R\left(t_a\left(f_a, f_\tau\right)\right)}{\partial t} + f_a = 0 . \quad (16)$$

Considering complexity of the range model, it is difficult to find a closed-form solution for the stationary point. Fortunately, the additional high-order terms are small [24]. We ignore the effect of the cubic term and quartic term, and use the stationary point of ESRM to derive the 2D PTS of the echo signal. The result is given by

$$S(f_\tau, f_a) = \sigma_0 \omega_a\left(t_a\left(f_a, f_\tau\right)\right) \cdot \omega_r\left(f_\tau\right) \cdot exp\left\{-\frac{j\pi f_\tau^2}{K_r}\right\}$$
$$\cdot exp\left\{-j4\pi P\left(f_\tau\right)\sqrt{\frac{4P\left(f_\tau\right)^2 v_0^2 r_0^2 sin\varphi_0^2}{4P\left(f_\tau\right)^2 v_0^2 - f_a^2} + \Theta_3 + \Theta_4}\right\}$$
$$\cdot exp\left\{\frac{j2\pi f_a^2 r_0 sin\varphi_0}{v_0\sqrt{4P\left(f_\tau\right)^2 v_0^2 - f_a^2}}\right\} \cdot exp\left\{\frac{-j2\pi r_0 f_a cos\varphi_0}{v_0}\right\}, \quad (17)$$

where

$$\begin{cases} P\left(f_\tau\right) = \left(\frac{1}{\lambda} + \frac{f_\tau}{c}\right) \\ \Theta_3 = \Delta a_3 t_a\left(f_a, f_\tau\right)^3 \\ \Theta_4 = \Delta a_4 t_a\left(f_a, f_\tau\right)^4 \\ t_a\left(f_a, f_\tau\right) = \frac{r_0 cos\varphi_0}{v_0} - \frac{r_0 f_a sin\varphi_0}{v_0\sqrt{4P(f_\tau)^2 v_0^2 - f_a^2}} . \end{cases} \quad (18)$$

In order to verify the accuracy of the 2D spectrum, a simulation is performed where the echo signal is compressed by the 2D spectrum based on MERSM/ERSM/DRM4/AERSM. The impulse response widths (IRW) (normalized to the theoretical
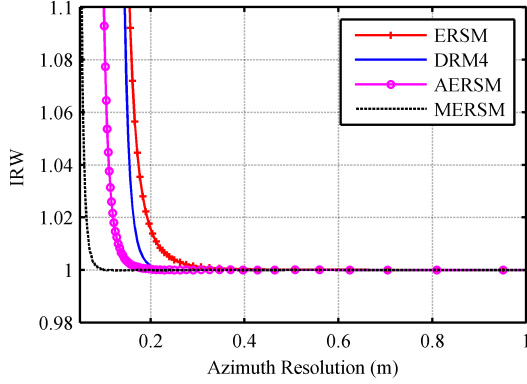
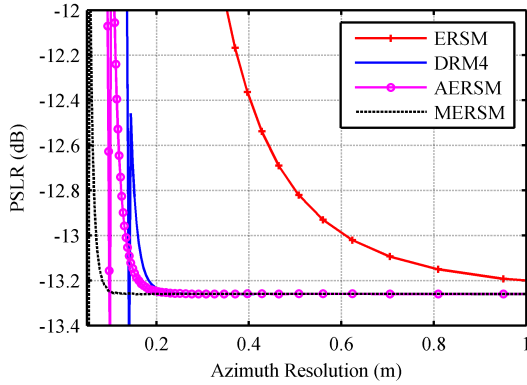Fig. 4. IRW as a function of azimuth resolution.

Fig. 5. PSLR as a function of azimuth resolution.

value) with respect to azimuth resolution are plotted in Fig. 4, and the peak side lobe ratios (PSLR) results are given in Fig. 5. We can see that the 2D PTS of MESRM is more accurate than others and an accurate signal spectrum can be obtained even if the azimuth resolution is up to 0.1m, which can meet the requirement of high resolution space-borne SAR.

III. HIGH-ORDER IMAGING ALGORITHM

Based on the proposed signal model in Section II, a novel imaging algorithm is presented in this section. The time-frequency diagrams at reference slant range is illustrated in Fig. 6, where B_T denotes the azimuth bandwidth of the point target that is much higher than PRF, B_{wave} is the instantaneous Doppler bandwidth, $B_{a,steer}$ is the Doppler bandwidth that results from beam steering.

For the imaging process, three problems emerge in the high resolution case. The first problem is the insufficient pulse repetition frequency (PRF) [25], [26]. In high resolution space-borne SAR, the steering of the antenna beam introduces extra bandwidth that may be several times the PRF. As a result, severe azimuth aliasing occurs, especially in the case of ultra-high resolution. The second problem is accurate focusing within the full swath [27]–[29]. As integration time increases with resolution, the space dependence of the 2D point scatterer response (PSR) becomes much more significant, which increases the difficulty for the following imaging
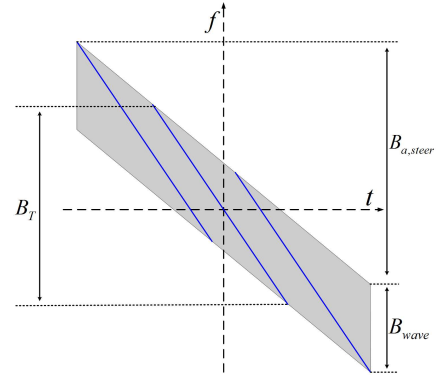

Fig. 6. Time frequency diagram of the sliding spotlight SAR.

process. The third problem is azimuth dimension folding in the focused domain [25]. After azimuth preprocessing, the azimuth sampling rate may increase, and the time scale may be compressed. As a result, image aliasing is likely to occur in azimuth.

Based on the above discussion, a novel high-order imaging algorithm is proposed here. The block diagram of our proposed algorithm is shown in Fig. 7. There are three parts: the first part is azimuth preprocessing, which is used to remove azimuth aliasing; the second part is high precision focusing within the full swath; the last part is re-sampling processing, which solves azimuth folding in the focused domain. In the following, details of the basic operations are provided according to the signal flow in the diagram.

A. Azimuth preprocessing

To remove azimuth aliasing, two methods are usually adopted: the two-step processing method [30]–[32], and the sub-aperture method [15], [25], [33]. The key point of the two-step processing method is that the convolution operation can be realized by two complex multiplications and one FFT in the discrete domain. Then azimuth aliasing can be avoided by scaling processing. However, in order to preserve the space variant characteristics of the signal, the reference function should be range independent, which will introduce extra residual azimuth bandwidth $B_{residual}$, given by [32]

$$B_{residual} = \left[\frac{(1 - H_f) v_s^2 T_s}{c r_0} + \frac{\theta_b v_s}{c} \right] B_r , \qquad (19)$$

where T_s is the echo acquisition time, B_r is the transmitted bandwidth, θ_b is the beam width, v_s is the velocity of the SAR sensor, and H_f denotes the hybrid factor, expressed as

$$H_f = \frac{r_{rot} - r_0}{r_{rot}} , \qquad (20)$$

with r_{rot} being the distance from the rotation point to the SAR sensor at Doppler center time.

According to equation (19), $B_{residual}$ is proportional to the transmitted bandwidth. With a large transmitted bandwidth, $B_{residual}$ will also lead to azimuth aliasing. Therefore, the two-step processing method is not suitable for the ultra-high resolution case.

For the sub-aperture method, it divides the raw data into

can be expressed as

$$B_{a,burst} = B_{wave} + B_{a,steer} + B_{a,v}$$
$$= B_{wave} + f_{r,rot}T_{sub} + \frac{B_r}{f_0}f_{d,k} , \qquad (21)$$

where $B_{a,v}$ is the variation of the Doppler centroid from the near to far range, $f_{d,k}$ is the Doppler centroid frequency of the k-th sub-aperture, $f_{r,rot}$ is the slope of the varying Doppler centroid introduced by beam steering, and T_{sub} is the size of the sub-aperture.

In the traditional sub-aperture method, sub-aperture azimuth FFT is performed after sub-aperture partition. To avoid aliasing, the size (in seconds) of the sub-aperture should meet the following condition [25]

$$T_{sub} \leq \frac{f_{prf} - B_{wave} - B_{a,v}}{f_{r,rot}} , \qquad (22)$$

where f_{prf} denotes the PRF. According to equations (21) and (22), the size of the sub-aperture decreases with increase of the transmitted bandwidth, reducing the efficiency of sub-aperture processing. In order to reduce the effect of the transmitted bandwidth, a "nonlinear shift method" is introduced to remove $B_{a,v}$ from equation (22) for a higher processing efficiency in [26]. After sub-aperture partition, the echo signal is transformed to the range frequency domain by range FFT. Then, nonlinear shift filtering is performed, with the filter function given by

$$H_1(f_\tau, t) = exp\left\{ -j2\pi \left\lfloor \left(1 + \frac{f_\tau}{f_0}\right) f_{d,k}T_{sub} \right\rfloor \frac{f_{prf}}{N_{burst}} t \right\} , \qquad (23)$$

where N_{burst} denotes the azimuth pixel number of the sub-aperture, and $\lfloor \cdot \rfloor$ is the rounding operation, which is used to ensure that the frequency shift is an integer multiple of the sampling interval, and then the nonlinear shift filtering can be compensated by spectrum shifting.

Next, a sub-aperture azimuth FFT is performed for a transformation into the 2D frequency domain. Before sub-aperture recombination, the different azimuth time shifts in the sub-apertures have to be equalized by multiplying with the function $H_2(f_\tau, k)$

$$H_2(f_\tau, k) = exp\left\{ -j2\pi \left\lfloor \left(1 + \frac{f_\tau}{f_0}\right) f_{d,k}T_{sub} \right\rfloor \frac{f_{prf}}{N_{burst}} t_{a,k} \right\} , \qquad (24)$$

where $t_{a,k}$ is the center time of the k-th sub-aperture.

Then, the individual sub-apertures can be combined together, and the 2D signal spectrum data is obtained in a discrete form without aliasing in the azimuth direction.

B. Data Focusing

Regarding the focusing operation of space-borne SAR, many algorithms have been proposed, such as CSA, RDA, FSA, and ωKA, etc [34]–[38]. However, they are not applicable to the ultra-high resolution case due to the complexity and space dependence of the 2D PTS. The hybrid correlation
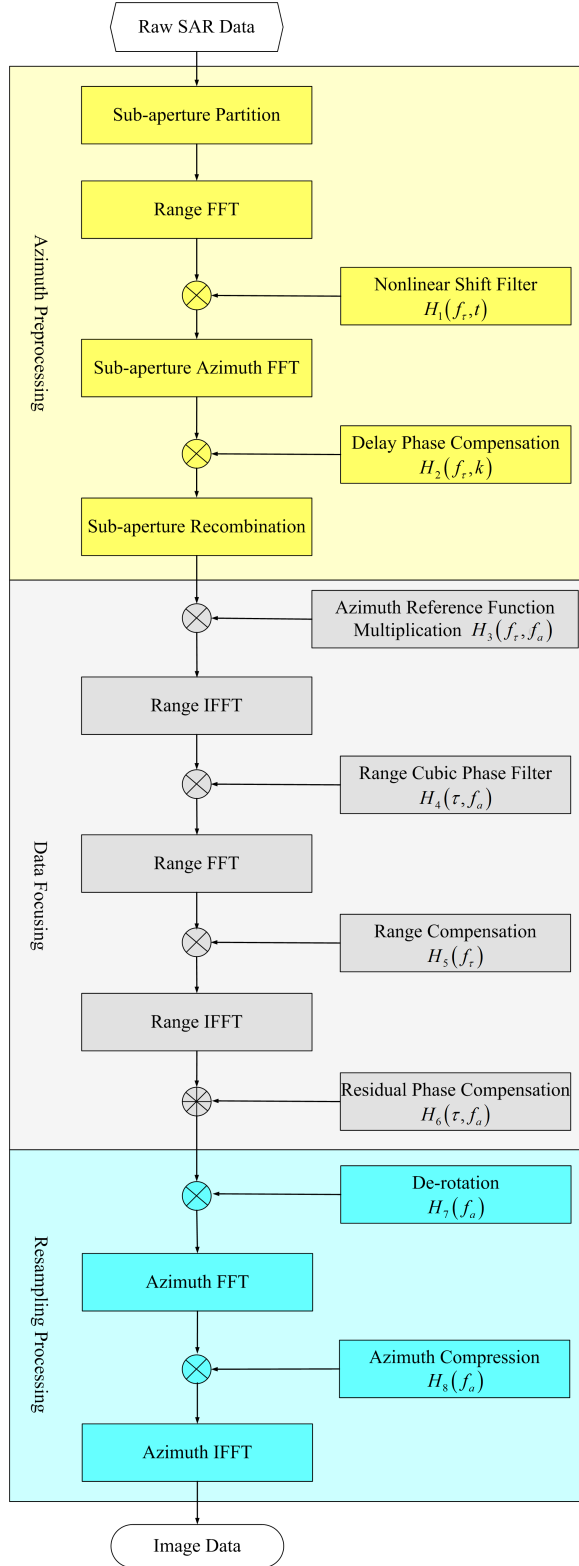

Fig. 7. Block diagram of the proposed high-order imaging algorithm.

separate blocks with the original range but smaller azimuth extension at the beginning of the processing in the 2D time domain [15]. After sub-aperture partition, the block bandwidth

algorithm is a simple imaging algorithm [39], where the reconstructed image is obtained by performing a 2D correlation between the echo signal and the complex conjugate of the reference function. However, with increase of the range cell migration (RCM), its efficiency decreases rapidly. Therefore, the conventional hybrid correlation algorithm is not suitable for the ultra-high resolution case either. In this section, an extended hybrid correlation algorithm is proposed. A coarse focusing step is introduced to reduce the effects caused by RCM, and then further refined focusing is performed by 2D correlation. The steps of the extended hybrid correlation algorithm are described as follows.

It starts with the azimuth reference function multiplication (RFM) in the 2D frequency domain to remove RCM, azimuth modulation and high-order cross-coupling at the reference slant range. The reference function is

$$
\begin{aligned}
H_3(f_\tau, f_a) = exp &\left\{ -\frac{j2\pi f_a^2 r_{ref} sin\varphi_{ref}}{v_{ref}\sqrt{4P(f_\tau)^2 v_{ref}^2 - f_a^2}} \right\} \\
\cdot exp &\left\{ j4\pi P(f_\tau)\sqrt{\frac{4P(f_\tau)^2 v_{ref}^2 r_{ref}^2 sin\varphi_{ref}^2}{4P(f_\tau)^2 v_{ref}^2 - f_a^2}} + \Theta_3 + \Theta_4 \right\} \\
\cdot exp &\left\{ \frac{j2\pi r_{ref} f_a cos\varphi_{ref}}{v_{ref}} \right\},
\end{aligned}
\tag{25}
$$

where r_{ref} is the reference slant range. The middle slant range is usually chosen as r_{ref}. The corresponding parameters are v_{ref}, φ_{ref}, $\Delta a_{3,ref}$, and $\Delta a_{4,ref}$.

After performing the range inverse fast Fourier transform (IFFT), the RCM, azimuth modulation and cross-coupling at the reference slant range are corrected. However, for the other range bins, some residual RCM and second-order cross-coupling is still present, which means that a longer correlation window in the range direction should be used for further refined focusing. To improve efficiency of the imaging algorithm, range cubic phase filter processing is introduced.

Similar to the chirp scaling principle, when a chirp signal multiplies with a cubic phase function, a small change of FM rate would be introduced, which is proportional to the position deviation of targets. If the change of FM rate introduced by the range cubic phase filter processing is equal to the deviation of the range FM rate at different range bins, the coarse focusing within the full swath can then be realized. Suppose the range cubic phase function is given by

$$
H_4(\tau, f_a) = exp\left\{ j\pi A(f_a; r_{ref})(\tau - \tau(f_a; r_{ref}))^3 \right\},
\tag{26}
$$

where

$$
\begin{cases}
\tau(f_a; r_{ref}) = \frac{2r_{ref} sin\varphi_{ref}}{c \cdot CS(f_a; r_{ref})} \\
DF(f_a; r_{ref}) = \left(\frac{\lambda f_a}{2v_{ref}} \right)^2 \\
CS(f_a; r_{ref}) = \sqrt{1 - DF(f_a; r_{ref})}.
\end{cases}
\tag{27}
$$

After the range cubic phase filtering operation, the new FM rate can be rewritten as follows

$$
\begin{aligned}
&K_{r,rn}(f_a; r_0) \\
&= K_{r,n}(f_a; r_0) + 3A(f_a; r_{ref}) \cdot (\tau(f_a; r_0) - \tau(f_a; r_{ref})),
\end{aligned}
\tag{28}
$$

where

$$
\begin{aligned}
\frac{1}{K_{r,n}(f_a; r_0)} = &\frac{1}{K_r} + 2r_0 sin\varphi_0 \frac{\lambda DF(f_a; r_0)}{c^2 CS(f_a; r_0)^3} \\
&- 2r_{ref} sin\varphi_{ref} \frac{\lambda DF(f_a; r_{ref})}{c^2 CS(f_a; r_{ref})^3}.
\end{aligned}
\tag{29}
$$

For $K_{r,rn}(f_a; r_0)$ to be equal to K_r, $A(f_a; r_{ref})$ should be selected as follows:

$$
\begin{aligned}
A(f_a; r_{ref}) &= \frac{(K_r - K_{r,n}(f_a; r_0))}{3(\tau(f_a; r_0) - \tau(f_a; r_{ref}))} \\
&\approx \frac{\lambda K_r^2 \cdot DF(f_a; r_{ref})}{3c \cdot CS(f_a; r_{ref})^2}.
\end{aligned}
\tag{30}
$$

Next, a range FFT is applied for a transformation back to the 2D frequency domain, and range matched filtering is employed to remove range modulation. The reference function is

$$
H_5(f_\tau) = exp\left\{ \frac{j\pi f_\tau^2}{K_r} \right\}.
\tag{31}
$$

After the range IFFT, range compression is performed and the RCM at the reference range is completely corrected. The following step is hybrid correlation processing, which is used to correct the residual RCM in the range Doppler domain. The reconstructed image is obtained by 2D correlation between the echo signal and the complex conjugate of the reference function. With completed range compression for all targets, a sliding window in the range direction is applied to reduce the effect of residual RCM. The offset of the correlation window is determined by the residual RCM $\Delta R_{res}(f_a; r_0)$, which at the slant range r_0 is given by

$$
\begin{aligned}
\Delta R_{ref}(f_a; r_0) = &\frac{c}{2}(\tau(f_a; r_0) - \tau(f_a; r_{ref})) - (r_0 - r_{ref}) \\
&+ \frac{3cA(f_a; r_{ref})}{4K_r}(\tau(f_a; r_0) - \tau(f_a; r_{ref}))^2.
\end{aligned}
\tag{32}
$$

In order to obtain an accurate result, a correlation window with sixteen points in the range direction is suggested for the high resolution case. The signal after hybrid correlation processing can be expressed as

$$
\begin{aligned}
&S'(\tau, f_a; r_0) \\
&= \sum_{i=1}^n S\left(\tau + \left(i - \frac{n}{2} + \left\lfloor \frac{2\Delta R_{res}(f_a; r_0)f_s}{c} \right\rfloor \right) \frac{1}{f_s}, f_a \right) \\
&\quad \cdot IFT_R\{H_6^*(f_\tau, f_a; r_0)\},
\end{aligned}
\tag{33}
$$

where n is the length of the correlation function in the range direction, f_s is the range sampling rate, $IFT_R\{\cdot\}$ denotes

the range inverse FT, and $H_6^* (\cdot)$ is the 2D range dependent azimuth response function at the slant range r_0, given by

$$H_6 (f_\tau, f_a; r_0) = exp \left\{ j2\pi f_\tau \left\lfloor \frac{2\Delta R_{res} (f_a; r_0) f_s}{c} \right\rfloor \frac{1}{f_s} \right\}$$
$$\cdot exp \left\{ j4\pi R_{ref} (t_0 (f_a; r_{ref})) P (f_\tau) \cdot \frac{K_r}{K_n} \right\}$$
$$\cdot exp \left\{ -j4\pi R_0 (t_0 (f_a; r_0)) P (f_\tau) \cdot \frac{K_r}{K_n} \right\}$$
$$\cdot exp \left\{ j\pi A (f_a; r_{ref}) \frac{f_\tau^3}{K_n^3} \right\} \cdot exp \left\{ j\pi A (f_a; r_{ref}) \Delta\tau^3 \right\}$$
$$\cdot exp \left\{ j3\pi A (f_a; r_{ref}) \Delta\tau \frac{f_\tau^2}{K_n^2} \right\} , \tag{34}$$

where

$$\Delta\tau = \tau (f_a; r_0) - \tau (f_a; r_{ref}) , \tag{35}$$
$$K_n = K_r + 3A (f_a; r_{ref}) \Delta\tau . \tag{36}$$

The first exponential term in (34) is used to compensate the offset of the correlation window. The second and third exponential terms are introduced to compensate the residual high-order phase error. The range cubic phase filtering is compensated by the next three exponential terms. After hybrid correlation processing, the residual RCM and the residual phase error are completely corrected.

C. Re-sampling

Because of sub-aperture processing in azimuth, aliasing is likely to occur after the azimuth inverse FFT. To avoid aliasing, the azimuth swath should meet the following condition [40]

$$Sw_a \leq \frac{N_{burst}}{f_{prf}} v_g = T_1 v_g , \tag{37}$$

where Sw_a denotes the swath width in the azimuth direction, v_g is the velocity of the antenna beam on the ground, and T_1 is the azimuth time of final image. However, in most cases, the above equation can not be satisfied. Therefore, an azimuth re-sampling operation is applied to overcome the constraint on the azimuth swath in equation (37) [40]. The operation begins with de-rotation processing, with the de-rotation phase function given by

$$H_7 (f_a) = exp \left\{ -j\pi \frac{H_f f_a^2}{f_{r,rot}} \right\} . \tag{38}$$

After the azimuth inverse FFT, quadric phase multiplication is introduced to compensate the residual quadric phase. Then the image is obtained by azimuth IFFT. The quadric phase function is given by

$$H_8 (t) = exp \left\{ -j\pi \frac{f_{r,rot} t^2}{H_f} \right\} . \tag{39}$$

IV. SIMULATIONS AND ANALYSES

In this section, simulations are performed to first verify the accuracy of the range cubic phase filter processing. Then, the performance of the proposed imaging algorithm is demonstrated. The simulation parameters are listed in Table I.

TABLE I
SIMULATION PARAMETERS

Description	Value	Units
Orbit Parameters		
Semi-major	514	km
Eccentricity	0.0011	-
Inclination	98	deg
Longtitude of ascend note	0	deg
Argument of perigee	90	deg
Radar Parameters		
Carrier frequency	9.6	GHz
Bandwidth	1.2	GHz
Sampling frequency	1.4	GHz
Look angle	30	deg
Antenna length	6.0	m
Target Parameters of Scene Center		
Azimuth resolution	0.25	m
Hybrid factor	0.08333	-
r_0 of scene center	599.86	km
f_d of scene center	20.320	Hz
f_r of scene center	-5812.134	Hz/s
f_{r3} of scene center	0.073554	Hz/s^2
f_{r4} of scene center	2.647627	Hz/s^3
Illuminated time	11.6	s

A. Validation of the range cubic phase filter

There are two steps in the focusing process of the proposed imaging algorithm: coarse focusing using RFM and further refined focusing by the hybrid correlation processing. However, considering the range dependence of the 2D PTS, there is a clear defocusing phenomenon at the edge of swath for ultra-high resolution space-borne SAR, as shown in Fig. 8. This means that a longer correlation window in the range direction should be used for further refined focusing, which will reduce the efficiency of the imaging algorithm. The range cubic phase filter is used to compensate the effect caused by the range dependence of the 2D PTS, and then the coarse focusing within the full swath can be realized by the RFM. In order to verify the validity of the range cubic phase filter processing, the echo signal of the edge target after the range cubic phase filter is compressed by the reference function in equation (31). The compression result is shown in Fig. 9. It can be seen that, after the range cubic phase filter, coarse focusing can be realized by RFM.

Another approximation of the algorithm is in the derivation of equation (34), where the deviation of the stationary point caused by $H_4 (\tau, f_a; R_{ref})$ is ignored. To assess the effect of this approximation, the echo signal after the range cubic phase filtering is compressed by the reference function in equation (34). The IRW (normalized to the theoretical value) with respect to transmitted bandwidth is shown in Fig. 10, and the PSLR result with respect to the transmitted bandwidth is shown in Fig. 11. The change of both IRW and PSLR is less than 1 ‰. So the effect of the approximation in the derivation of equation (34) is extremely small, and can be ignored in the following processing.
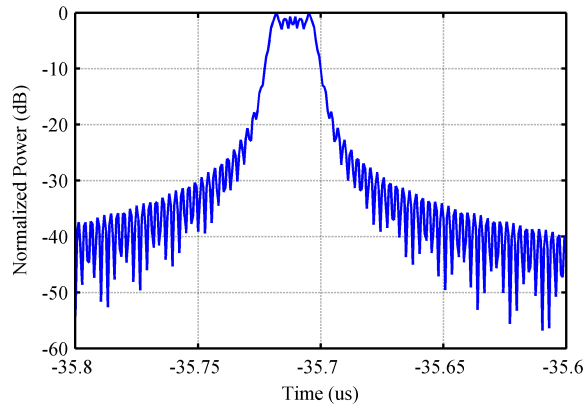
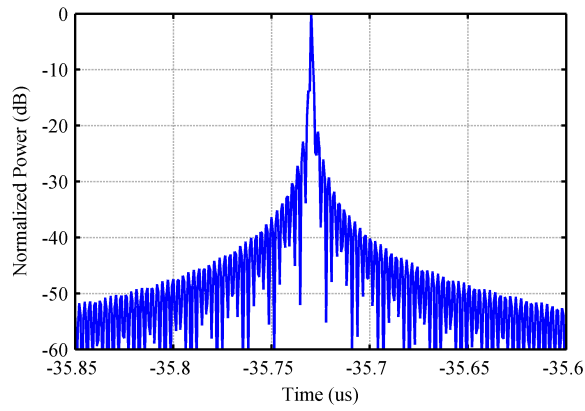Fig. 8. Compression result before the range cubic phase filter.

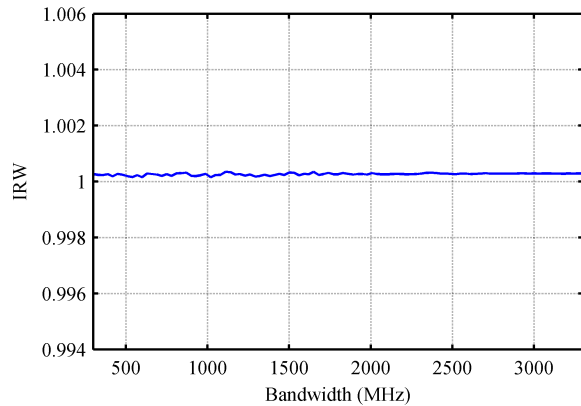Fig. 9. Compression result after the range cubic phase filter.

Fig. 10. IRW with respect to transmitted bandwidth.

B. Simulation for the imaging algorithm

The simulated scene is shown in Fig. 12 , where the distances of different targets along range and azimuth are 10.0 km and 2.0 km, respectively. First, the focused results of the NCS algorithm and the ωk algorithm are shown in Fig. 13 and Fig. 14 for comparison, where ESRM is used and the corresponding parameters are calculated according to (2) for each range bin. It can be seen that the focused results suffer from severe degradation, especially those at the top and bottom sides of the scene.
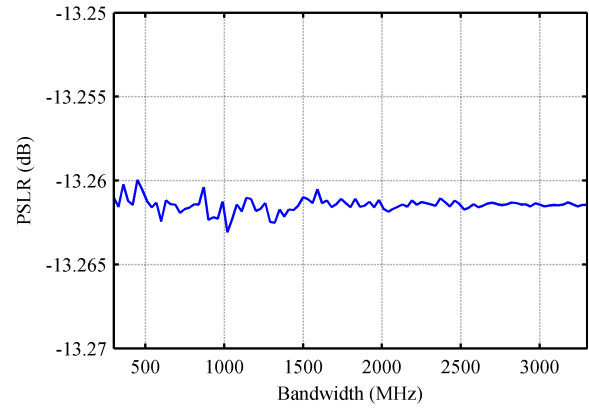

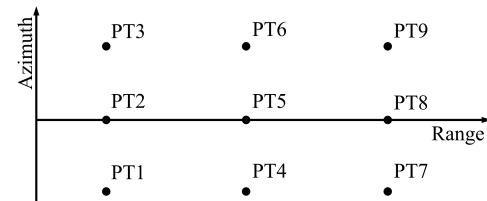Fig. 11. RSLR with respect to transmitted bandwidth.

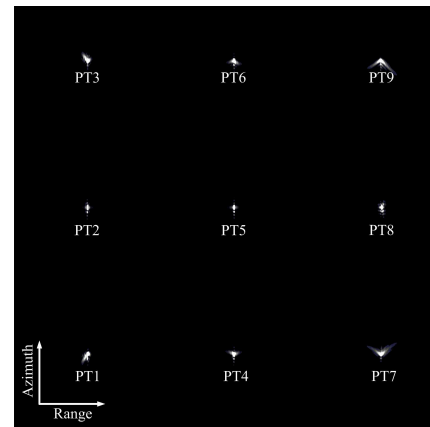Fig. 12. Ground scene for simulation.

Fig. 13. result by the NCS algorithm.

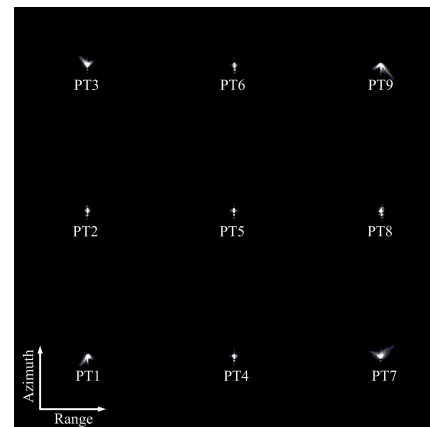Fig. 14. Focused result by the ωk algorithm.
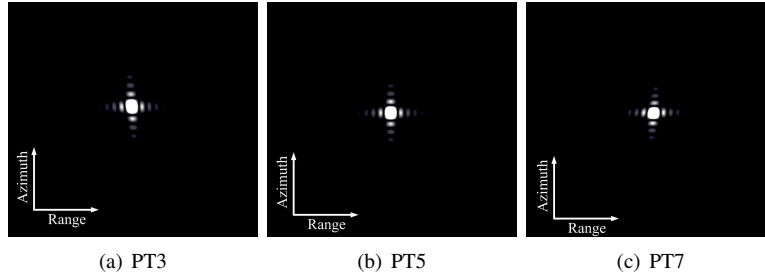
(a) PT3   (b) PT5   (c) PT7

Fig. 16. Interpolated results of PT3, PT5, and PT7 by the proposed algorithm
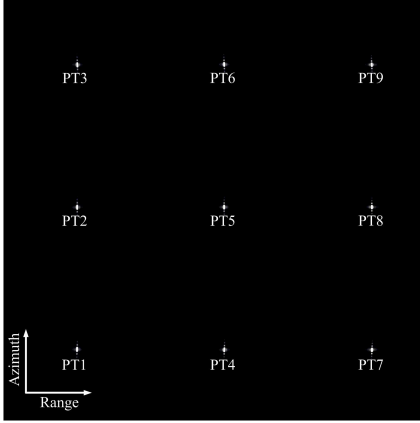

Fig. 15. Focused result by the proposed algorithm.

Fig. 15 shows the focused result based on our proposed algorithm. The interpolated contours of PT3, PT5, and PT7 are presented in Fig. 16 to evaluate the image quality. Compared to the NCS algorithm result and the ωk algorithm result, the focusing performance has been improved significantly. All of the targets are well compressed by the proposed method. To quantify the focusing performance, the point target analysis results are listed in Table II, where the ideal PSLR and the integrated side lobe ratio (ISLR) are respectively 13.26 dB and 9.68 dB using the rectangular window. The theoretical resolution is calculated according the following equation

$$\begin{cases} \rho_r = 0.886 \cdot \frac{c}{2B_r} \\ \rho_{a,r_0} = \frac{A_L}{2} \frac{H_f \cdot r_0 + r_{ref} - r_0}{r_{ref}}, \end{cases} \tag{40}$$

where A_L is the antenna length.

According to Table II, it can be seen that the deterioration of the IRW in the range direction is less than 1% and that in the azimuth direction is less than 2%. The PSLRs shows less than 3% degradation both in the azimuth and range direction. All these indicate that the corresponding focusing algorithm can meet the imaging requirement of the high resolution space-borne SAR effectively.

Location is another index to evaluate the performance of imaging algorithms. Table III shows the position deviations of all targets after being compressed, where the slant range imaging plane is taken as the reference plane. We can see that the position deviation in both the range and azimuth directions is less than 0.05m, showing a high Location accuracy for our proposed algorithm.

TABLE II
PERFORMANCE ANALYSIS OF POINT TARGETS

	Range				Azimuth			
	$\rho_{r,m}$ (m)	$\rho_{r,c}$ (m)	PSLR (dB)	ISLR (dB)	$\rho_{a,m}$ (m)	$\rho_{a,c}$ (m)	PSLR (dB)	ISLR (dB)
1	0.112	0.111	13.21	-10.01	0.276	0.275	13.23	10.68
2	0.111	0.111	13.26	-10.64	0.276	0.275	13.33	10.66
3	0.111	0.111	13.09	-9.87	0.279	0.275	13.32	10.68
4	0.111	0.111	13.27	-9.95	0.251	0.250	13.20	10.62
5	0.111	0.111	13.25	-9.95	0.252	0.250	13.32	10.65
6	0.111	0.111	13.26	-9.95	0.251	0.250	13.37	10.65
7	0.111	0.111	13.10	-9.89	0.226	0.225	13.22	10.64
8	0.111	0.111	13.21	-9.95	0.226	0.225	13.22	10.63
9	0.110	0.111	13.07	-10.37	0.226	0.225	13.00	10.69

TABLE III
LOCATION RESULTS OF POINT TARGETS

Point Targets	Position in imaging scene (m)	Position in focued scene (m)	Position deviation (m)
PT1	(594505.52,-1948.64)	(594505.54,-1948.67)	(0.02,-0.03)
PT2	(594517.57, 45.81)	(594517.58, 45.77)	(0.01,-0.04)
PT3	(594529.70, 2036.73)	(594529.70, 2036.77)	(0.00, 0.04)
PT4	(599849.72,-1987.40)	(599849.70,-1987.38)	(-0.02,-0.02)
PT5	(599860.22, 0.00)	(599860.20, -0.00)	(0.02, 0.00)
PT6	(599870.81, 1994.45)	(599870.80, 1994.42)	(-0.01,-0.03)
PT7	(605323.63,-2012.06)	(605323.63,-2012.06)	(0.00, 0.00)
PT8	(605332.50, -21.14)	(605332.51, -21.14)	(0.01, 0.00)
PT9	(605341.45, 1969.78)	(605341.47, 1969.81)	(0.02, 0.03)

V. CONCLUSION

For ultra-high resolution space-borne SAR, a novel high-order range equation model called MERSM has been proposed in this paper, which accounts well for actual range history variations up to the quartic term by incorporating equivalent radar acceleration into the equivalent squint range model. As a result, a higher azimuth resolution can be accommodated by this model. Furthermore, the signal model as well as PTS has been provided. Based on the signal model, a high-order imaging algorithm has been developed, where improved sub-aperture processing is introduced to remove azimuth aliasing, and accurate focusing is achieved by an extended hybrid correlation algorithm. Simulation results have been provided to verify the effectiveness of the proposed model and the corresponding imaging algorithm.

References

[1] W. Townsend, "An initial assessment of the performance achieved by the Seasat-1 radar altimeter," *IEEE Journal of Oceanic Engineering*, vol. 5, no. 2, pp. 80–92, Apr. 1980.

[2] I. J. Birrer, E. M. Bracalente, G. J. Dome, J. Sweet and G. Berthold, "σ Â Signature of the Amazon Rain Forest Obtained from the Seasat Scatterometer," *IEEE Transactions on Geoscience and Remote Sensing*, vol. GE-20, no. 1, pp. 11–17, Jan. 1982.

[3] F. Covello, F. Battazza, A. Coletta, E. Lopinto, C. Fiorentino, L. Pietranera, G. Valentini and S. Zoffoli, "COSMO-SkyMed an existing opportunity for observing the Earth," *Journal of Geodynamics*, vol. 49, no. 3, pp. 171–180, Apr. 2010.

[4] W. Pitz and D. Miller, "The terraSAR-X satellite," *IEEE Transactions on Geoscience and Remote Sensing*, vol. 48, no. 2, pp. 615–622, Feb. 2010.

[5] R. Werninghaus and S. Buckreuss, "The TerraSAR-X mission and system design," *IEEE Transactions on Geoscience and Remote Sensing*, vol. 48, no. 2, pp. 606–614, Feb. 2010.

[6] S. Lehner and J. Schulz-Stellenfleth, "TerraSAR-X for Oceanography," in *Proc. IEEE International Geoscience and Remote Sensing Symposium*, 2006, pp. 1342–1345.

[7] H. Breit, T. Fritz, U. Balss, M. Lachaise, A. Niedermeier and M. Vonavka, "TerraSAR-X SAR processing and products," *IEEE Transactions on Geoscience and Remote Sensing*, vol. 48, no. 2, pp. 727–740, Feb. 2010.

[8] S. Lehner, J. Horstmann, and J. Schulz-Stellenfleth, "TerraSAR-X for oceanography mission overview," in *Proc. IEEE International Geoscience and Remote Sensing Symposium*, 2004, pp. 3303–3306.

[9] S. Mezzasoma, A. Gallon, F. Impagnatiello, G. Angino, S. Fagioli, A. Capuzi, F. Caltagirone, R. Leonardi and U. Ziliotto, "COSMO-SkyMed system commissioning: end-to-end system performance verification," in *Proc. IEEE Radar Conference*, 2008, pp. 1–5.

[10] A. Torre, D. Calabrese and M. Porfilio, "COSMO-SkyMed: Image quality achievements," in *Proc. International Conference on Recent Advances in Space Technologies*, 2011, pp. 861–864.

[11] F. Covello, F. Battazza, A. Coletta, G. Manoni, and G. Valentini, "COSMO-SkyMed mission status: Three out of four satellites in orbit," in *Proc. IEEE International Geoscience and Remote Sensing Symposium*, 2009, pp. 773–776.

[12] J. Janoth, S. Gantert, W. Koppe, A. Kaptein, and C. Fischer, "TerraSAR-X2-Mission overview," in *Proc. IEEE International Geoscience and Remote Sensing Symposium*, 2012, pp. 217–220.

[13] J. Janoth, S. Gantert, T. Schrage and A. Kaptein, "TerraSAR Next Generation Mission Capabilities," in *Proc. IEEE International Geoscience and Remote Sensing Symposium*, 2013, pp. 2297–2300.

[14] C. Cafforio, C. Prati, and F. Rocca, "SAR data focusing using seismic migration techniques," *IIEEE Transactions on Aerospace and Electronic Systems*, vol. 27, no. 2, pp. 194–207, Mar. 1991.

[15] J. Mittermayer, A. Moreira, and O. Loffeld, "Spotlight SAR data processing using the frequency scaling algorithm," *IEEE Transactions on Geoscience and Remote Sensing*, vol. 37, no. 5, pp. 2198–2214, Sep. 1999.

[16] X. Sun, T. Yeo, C. Zhang, Y. Lu and P. Kooi, "Time-varying step-transform algorithm for high squint SAR imaging," *IEEE Transactions on Geoscience and Remote Sensing*, vol. 37, no. 6, pp. 2668–2677, Nov. 1999.

[17] L. Huang, X. Qiu, D. Hu and C. Ding, "Focusing of medium-earth-orbit SAR with advanced nonlinear chirp scaling algorithm," *IEEE Transactions on Geoscience and Remote Sensing*, vol. 49, no. 1, pp. 500–508, Jan. 2011.

[18] K. Eldhuset, "A new fourth-order processing algorithm for spaceborne SAR," *IEEE Transactions on Aerospace and Electronic Systems*, vol. 34, no. 3, pp. 824–835, Jul. 1998.

[19] K. Eldhuset, "Ultra high resolution spaceborne SAR processing with EETF4," in *Proc. IEEE International Geoscience and Remote Sensing Symposium*, 2001, pp. 2689–2691.

[20] K. Eldhuset, "Spaceborne bistatic SAR processing using the EETF4 algorithm," *IEEE Geoscience and Remote Sensing Letters*, vol. 6, no. 2, pp. 194–198, Apr. 2009.

[21] K. Eldhuset, "Ultra high resolution spaceborne SAR processing," *IEEE Transactions on Aerospace and Electronic Systems*, vol. 40, no. 1, pp. 370–378, Jan. 2004.

[22] Y. Neo, F. H. Wong and I. G. Cumming, "A comparison of point target spectra derived for bistatic SAR processing," *IEEE Transactions on Geoscience and Remote Sensing*, vol. 46, no. 9, pp. 2481–2492, Sep. 2008.

[23] F. H. Wong, I. G. Cumming and Y. Neo, "Focusing bistatic SAR data using the nonlinear chirp scaling algorithm," *IEEE Transactions on Geoscience and Remote Sensing*, vol. 46, no. 9, pp. 2493–2505, Sep. 2008.

[24] G. W. Davidson, I. G. Cumming and M. R. Ito, "A chirp scaling approach for processing squint mode SAR data," *IEEE Transactions on Aerospace and Electronic Systems*, vol. 32, no. 1, pp. 121–133, Jan. 1996.

[25] P. Prats, R. Scheiber, J. Mittermayer, A. Meta and A. Moreira, "Processing of sliding spotlight and TOPS SAR data using baseband azimuth scaling," *IEEE Transactions on Geoscience and Remote Sensing*, vol. 48, no. 2, pp. 770–780, Feb. 2010.

[26] D. An, X. Huang, T. Jin and Z. Zhou, "Extended two-step focusing approach for squinted spotlight SAR imaging," *IEEE Transactions on Geoscience and Remote Sensing*, vol. 50, no. 7, pp. 2889–2900, Jul. 2012.

[27] F. He, Q. Chen, Z. Dong and Z. Sun, "Processing of Ultrahigh-Resolution Spaceborne Sliding Spotlight SAR Data on Curved Orbit," *IEEE Transactions on Aerospace and Electronic Systems*, vol. 49, no. 2, pp. 819–839, Apr. 2010.

[28] T. Zeng, W. Yang, Z. Ding and L. Liu, "Advanced range migration algorithm for ultra-high resolution spaceborne synthetic aperture radar," *IET Radar, Sonar & Navigation*, vol. 7, no. 7, pp. 764–772, Aug. 2013.

[29] Y. Luo, B. Zhao, X. Han, R. Wang, H. Song and Y. Deng, "A Novel High-Order Range Model and Imaging Approach for High-Resolution LEO SAR," *IEEE Transactions on Geoscience and Remote Sensing*, vol. 52, no. 7, pp. 3473–3485, Jun. 2014.

[30] R. Lanari, M. Tesauro, E. Sansosti and G. Fornaro, "Spotlight SAR data focusing based on a two-step processing approach," *IEEE Transactions on Geoscience and Remote Sensing*, vol. 39, no. 9, pp. 1993–2004, Sep. 2001.

[31] P. Wang, Y. Zhou, J. Chen, C. Li, Z. Yu and M. He, "A deramp frequency scaling algorithm for processing space-borne spotlight SAR data," in *Proc. IEEE International Geoscience and Remote Sensing Symposium*, 2006, pp. 3148–3151.

[32] F. Liu, Z. Ding, T. Zeng and T. Long, "Performance analysis of two-step algorithm in sliding spotlight space-borne SAR," in *Proc. IEEE Radar Conference*, 2010, pp. 965–968.

[33] P. Prats, R. Scheiber, J. Mittermayer, A. Meta, A. Moreira and J. Sanz-Marcos, "A SAR processing algorithm for TOPS imaging mode based on extended chirp scaling," in *Proc. IEEE International Geoscience and Remote Sensing Symposium*, 2007, pp. 148–151.

[34] R. K. Raney, H. Runge, R. Bamler, I. G. Cumming and F. H. Wong, "Precision SAR processing using chirp scaling," *IEEE Transactions on Geoscience and Remote Sensing*, vol. 32, no. 4, pp. 786–799, Jul. 1994.

[35] A. Moreira and Y. Huang, "Airborne SAR processing of highly squinted data using a chirp scaling approach with integrated motion compensation," *IEEE Transactions on Geoscience and Remote Sensing*, vol. 32, no. 5, pp. 1029–1040, Sep. 2002.

[36] A. Moreira, J. Mittermayer and R. Scheiber, "Extended chirp scaling algorithm for air- and spaceborne SAR data processing in stripmap and ScanSAR imaging modes," *IEEE Transactions on Geoscience and Remote Sensing*, vol. 34, no. 5, pp. 1123–1136, Sep. 2002.

[37] A. Reigber, E. Alivizatos, A. Potsis and A. Moreira, "Extended wavenumber-domain synthetic aperture radar focusing with integrated motion compensation," *IET Radar, Sonar & Navigation*, vol. 153, no. 3, pp. 301–310, Jun. 2006.

[38] P. Prats, R. Scheiber, M. Rodriguez-Cassolar, S. Wollstadt, J. Mittermayer, B. Brautigam, M. Schwerdt, A. Reigber and A. Moreira, "High precision SAR focusing of TerraSAR-X experimental staring spotlight data," in *Proc. IEEE International Geoscience and Remote Sensing Symposium*, 2012, pp. 3576–3579.

[39] C. Wu, K. Y. Liu and M. Jin, "Modeling and a correlation algorithm for spaceborne SAR signals," *IEEE Transactions on Aerospace and Electronic Systems*, vol. AES-18, no. 5, pp. 563–575, Sep. 1982.

[40] W. Yang, J. Chen, H. Zeng, J. Zhou, P. Wang and C. Li, "A novel three-step image formation scheme for unified focusing on spaceborne SAR data," *Progress In Electromagnetics Research*, vol. 137, pp. 621–642, 2013.

Pengbo Wang received the Ph.D. degree in information and communication engineering from Beihang University (Beijing University of Aeronautics and Astronautics, BUAA), Beijing, China, in 2007. From 2007 to 2010, he worked as a postdoc in the School of Electronics and Information Engineering, Beihang University. Since July 2010, he has been with the school of Electronics and Information Engineering, Beihang University (BUAA), as a lecturer. He has now authored and co-authored more than 40 journal and conference publications, and he is the holder of 10 patents in the field of microwave remote sensing. His current research interests include high-resolution spaceborne SAR image formation, novel techniques for spaceborne SAR systems and multimodal remote sensing data fusion.

Wei Yang was born in Hubei province, China, in 1983. He received the M.S. and Ph.D. degrees in signal and information processing from Beihang University (BUAA), China, in 2008 and 2011, respectively. In 2005, he studied the inner calibration signal analysis in SAR system. From 2006 2010, he focused on the system performance analysis and signal processing of high resolution and wide swath mode in spaceborn SAR, including the multi-channels TOPS mode and ScanSAR mode. From 2011, he is a postdoctoral with the School of Electronics and Information Engineering, Beihang University. His current research interests included ultra-high-resolution spaceborne SAR image formation, modeling and data simulation, as well as novel techniques for spaceborne SAR systems.

Wei Liu (S'01-M'04-SM'10) received his B.Sc. in Space Physics (minor in Electronics) in 1996, L.L.B. in Intellectual Property Law in 1997, both from Peking University, China, M.Phil. from the Department of Electrical and Electronic Engineering, University of Hong Kong, in 2001, and Ph.D. in 2003 from the School of Electronics and Computer Science, University of Southampton, UK. He then worked as a postdoc in the same group and later in the Communications and Signal Processing Group, Department of Electrical and Electronic Engineering, Imperial College London. Since September 2005, he has been with the Communications Research Group, Department of Electronic and Electrical Engineering, University of Sheffield, UK, as a lecturer. His research interests are mainly in sensor array signal processing, blind signal processing, multirate signal processing and their various applications in wireless communications, sonar, radar, satellite navigation, speech enhancement and biomedical engineering. He has now authored and co-authored more than 140 journal and conference publications, and a research monograph about wideband beamforming ("Wideband Beamforming: Concepts and Techniques", John Wiley & Sons, March 2010).
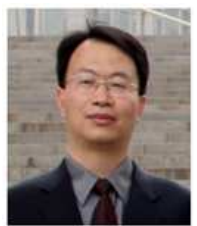
Jie Chen (M06) received the B.S. and Ph.D. degrees in information and communication engineering from Beihang University (Beijing University of Aeronautics and Astronautics, BUAA), Beijing, China, in 1996 and 2002, respectively. His Ph.D. study was focused on novel spaceborne synthetic aperture radar (SAR) system modeling and signal processing. From 2004, he was an associate professor with the School of Electronics and Information Engineering, Beihang University (BUAA). He was awarded New Century Excellent Talents in University, (NCET), by Ministry of Education, China, in 2006, and Excellent Young Teachers in University, by Fok Ying Tong Education Foundation and Ministry of Education, China, in 2008, respectively. He was a Visiting Researcher at the School of Mathematics and Statistics, University of Sheffield, Sheffield, UK, from 2009 to 2010, working with Prof. Shaun Quegan on ionospheric effects on low-frequency space radars that measure forest biomass and ionospheric electron densities. Dr. Chen is a full professor with the School of Electronics and Information Engineering, Beihang University (BUAA) from 2011. He has published more than 60 journal and conference papers, and he is the holder of 12 patents in the field of microwave remote sensing. His current research interests include multimodal remote sensing data fusion; topside ionosphere exploration with spaceborne HF/VHF-SAR system; high-resolution spaceborne SAR image formation and SAR image quality enhancement.